Closing the Surface Bandgap in Thin Bi_2Se_3/Graphene Heterostructures

Jimin Chae,[†] Seoung-Hun Kang,[‡] Sang Han Park,[†, §] Hanbum Park,[†] Kwangsik Jeong,[†] Tae Hyeon Kim,[†] Seok-Bo Hong,[†] Keun Su Kim,[†] Young-Kyun Kwon,[‡, ⊥] Jeong Won Kim,[▽] Mann-Ho Cho[*,†]

[†] Department of Physics, Yonsei University, Seoul, 03722, Korea

‡ Korea Institute for Advanced Study, Hoegiro 85, Seoul 02455, Korea

§ Pohang Accelerator Laboratory, POSTECH, Pohang 790-784, Korea

⊥ Department of Physics and Research Institute for Basic Sciences, Kyung-Hee University, Seoul, Korea

▽ Division of Industrial Metrology, Korea Research Institute of Standards and Science, Korea

[*] Corresponding author. Tel.: +82 2 2123 5610. E-mail address: mh.cho@yonsei.ac.kr (M.-H. Cho).

Supporting Information

1. Sample thickness

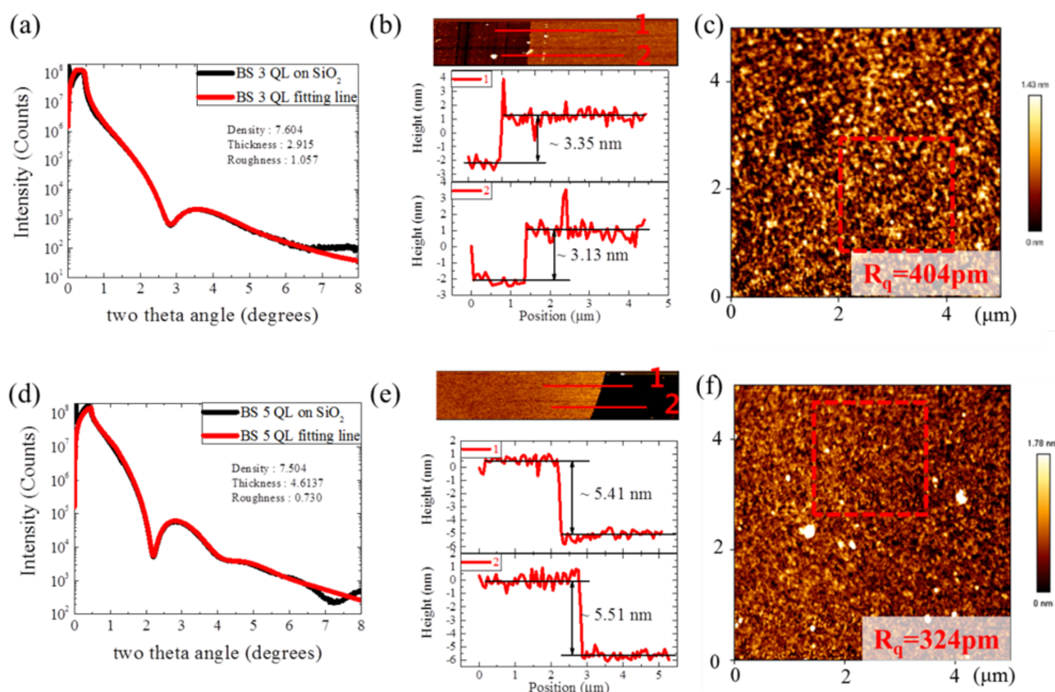

Figure S1. Thickness measurements using X-ray reflectivity (XRR) and atomic force microscope (AFM) for the Bi_2Se_3 films grown on SiO_2 substrate. (a)–(c) XRR data, AFM line profile and surface morphology for 3 QL Bi_2Se_3 films. (d)–(f) XRR data, AFM line profiles, and surface morphology for 5 QL Bi_2Se_3 films.

To confirm the thickness of the Bi_2Se_3 films grown on SiO_2 substrate, we conducted XRR and AFM measurements. We used the X-ray source of Cu Ka for XRR measurements and made a step edge by scratching the film for AFM line profiles. In XRR data, the densities of Bi_2Se_3 films were found to be 7.604 and 7.504 g/cm^3, similar to the reported values of 7.6 g/cm^3. The thicknesses values of Bi_2Se_3 films were 2.915 nm and 4.614 nm. Although there were some differences between the measured and expected thickness of Bi_2Se_3 films, it is sufficient to decide the thicknesses of the films to be 3 QLs and 5 QLs. In the AFM measurements (figures S1 (b) and (e), thicknesses of Bi_2Se_3 of 3 QL and 5 QL are 3.24 nm and 5.46 nm, respectively. The values obtained using AFM were higher than those obtained using XRR. This difference between the two measurement methods is reasonable because the step edge for AFM line profile was made by using a cutter. In conclusion, the thicknesses of the

films were in good agreement with the expected thickness of 3 QL and 5 QL.

2. Thickness-dependent ARPES data

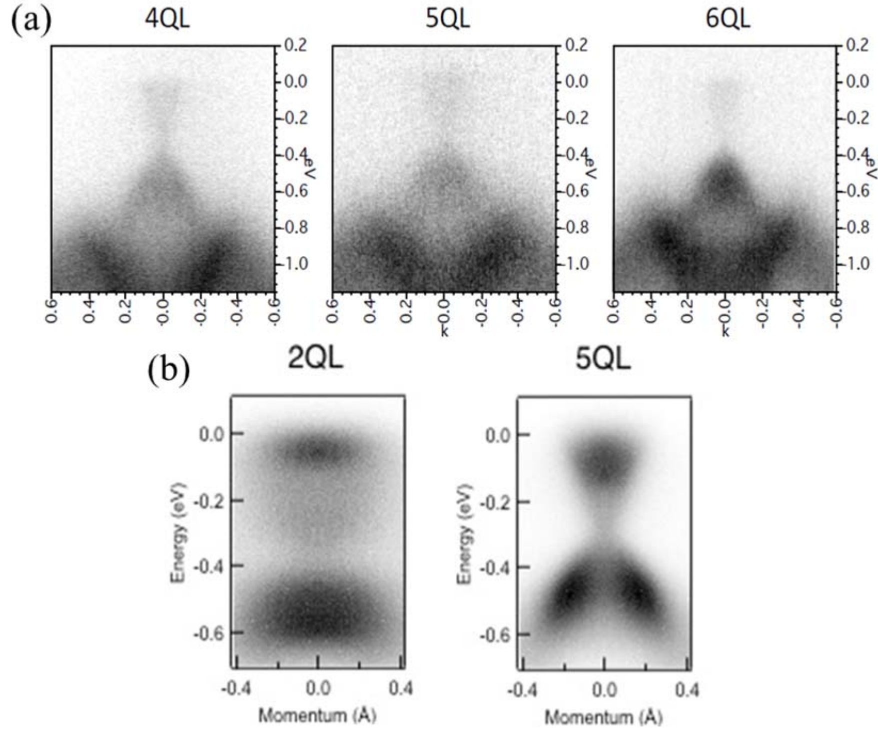

Figure S2. ARPES data for the Bi_2Se_3 film with different thicknesses. (a) 4–6 QL films are measured with a photon energy of 48 eV. (b) 2 and 5 QL films are measured with a photon energy of 21.2 eV

We conducted additional ARPES, varying the Bi_2Se_3 film thickness grown on the graphene substrate. A gradual Fermi level shift is shown as the thickness decreases from 6 QL to 4 QL at the photon energy of 34 eV, and there is no bandgap of surface states. Using the labsource, the bandgap at approximately 100 meV is shown in 2 QL Bi_2Se_3 films on the graphene/SiC substrate, implying the 2 QL film shows a bandgap reduction compared with reported data because of the strain and band bending effects, as discussed in the manuscript[1].

3. TEM images of Bi_2Se_3 grown on graphene

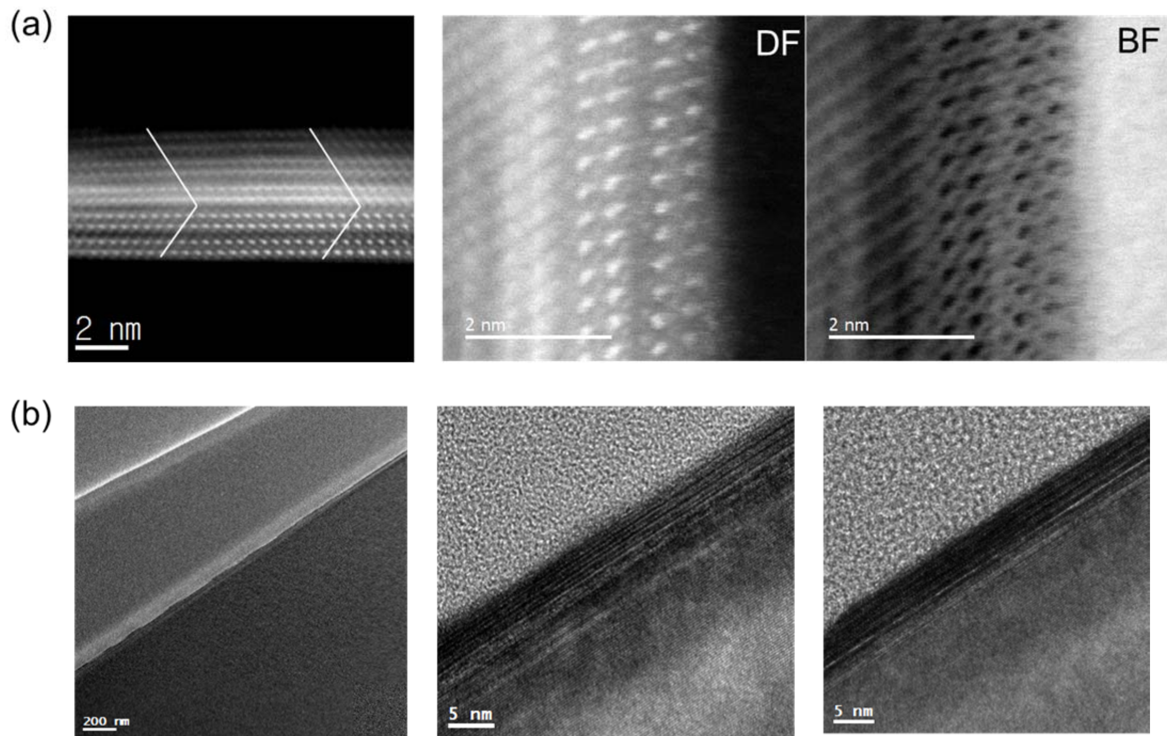

Figure S3. (a) STEM image of 5 QL Bi_2Se_3 on graphene/SiO_2 substrate and (b) HR-image of 4 QL Bi_2Se_3 on graphene/SiC

We obtained scanning tunneling electron microscope images for 5 QL Bi_2Se_3 on a graphene/SiO_2 substrate, as shown in figure S3 (a). The atomic alignment is observed clearly, showing a typical lamella structure[2]. In addition, we confirmed the macroscopic quality of the 4 QL Bi_2Se_3 grown on the monolayer graphene/SiC substrate, as shown in figure S3 (b). The film is flat and has a sharp morphology.

4. Comparing the SiO_2 and SiC as a substrate

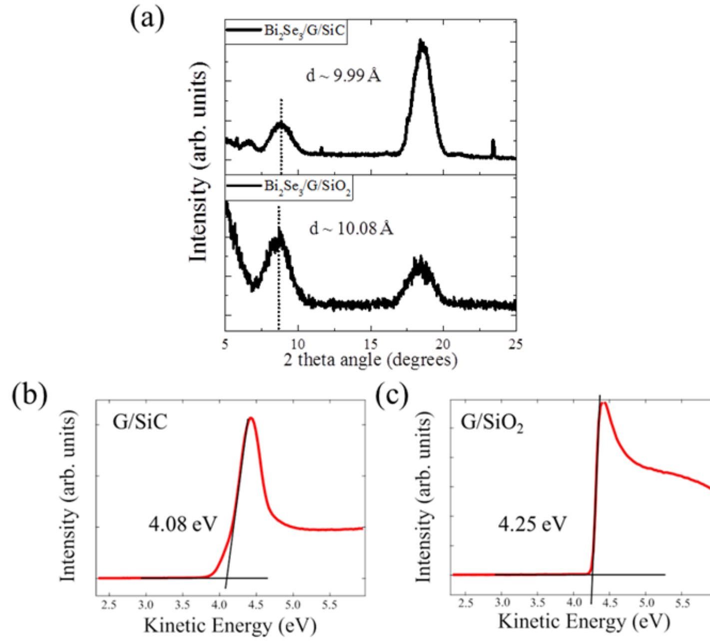

Figure S4. (a) XRD patterns of 3QL Bi_2Se_3/graphene/SiC and 3QL Bi_2Se_3/graphene/SiO_2 and workfunctions of (b) graphene/SiC and (c) graphene/SiO_2

Using ARPES measurement, we observed closing bandgap in 3QL Bi_2Se_3 grown on the graphene on SiC substrate. Using XPS, SAXS, and PPMS, we obtained various electrical and structural data on the film grown on graphene on SiO_2 substrate. In order to confirm the difference between the two films grown on the substrates, we compared the crystalline structure of Bi_2Se_3 using XRD and workfunction of the graphene on SiC and SiO_2 using UPS, as shown in figure S4. There are clear peaks of (003) and (006) in both film. In particular, the clear oscillation peak of (003) and higher intensity of (006) peak in 3 QL Bi_2Se_3/graphene/SiC sample implies that Bi_2Se_3/graphene/SiC has higher crystalline quality than the Bi_2Se_3/graphene/SiO_2 because of the higher quality of graphene epitaxially grown on SiC compared with graphene transferred on SiO_2. The d-spacings of the two samples calculated by (003) peaks are 0.999 nm and 1.008 nm for the Bi_2Se_3/graphene/SiC and Bi_2Se_3/graphene/SiO_2, respectively. This implies that Bi_2Se_3 films on both graphene/SiC and graphene/SiO_2 have a strain of approximately 5 %, which was obtained in SAXS data as shown in figure 2 (b). The film grown on graphene/SiC has less tensile strain than that grown on graphene/SiO_2.

However, the strain difference between Bi_2Se_3 films grown on graphene/SiC and graphene/SiO_2 does not affect our discussion, because this difference is not large (~0.8%) and the graphene causes the same strain effects to decrease tensile strain in the out-of-plane direction in the Bi_2Se_3 films. Furthermore, we compared the workfunctions of two graphene samples prepared on SiO_2 substrate and SiC substrate. The workfunctions of graphene grown on SiC substrate and transferred on SiO_2 were 4.08 and 4.25 eV, as shown below in figure S4. Considering that the workfunctions of Bi_2Se_3 film is 5.07 eV, as we discussed in supporting information, the differences in workfunction between Bi_2Se_3 and graphenes on both substrates are large enough to induce the strong band bending effects. In addition, the difference between graphene (~ 0.5 eV) and Bi_2Se_3 film (~ -0.25 eV) in simulated data, as shown in figure 3 (b) and (c), is similar to measured data. Therefore, the difference between the substrates on which we prepared graphene does not affect the discussions in the manuscript.

5. Spatial distribution of unstrained Bi_2Se_3 and Bi_2Se_3/graphene heterostructures

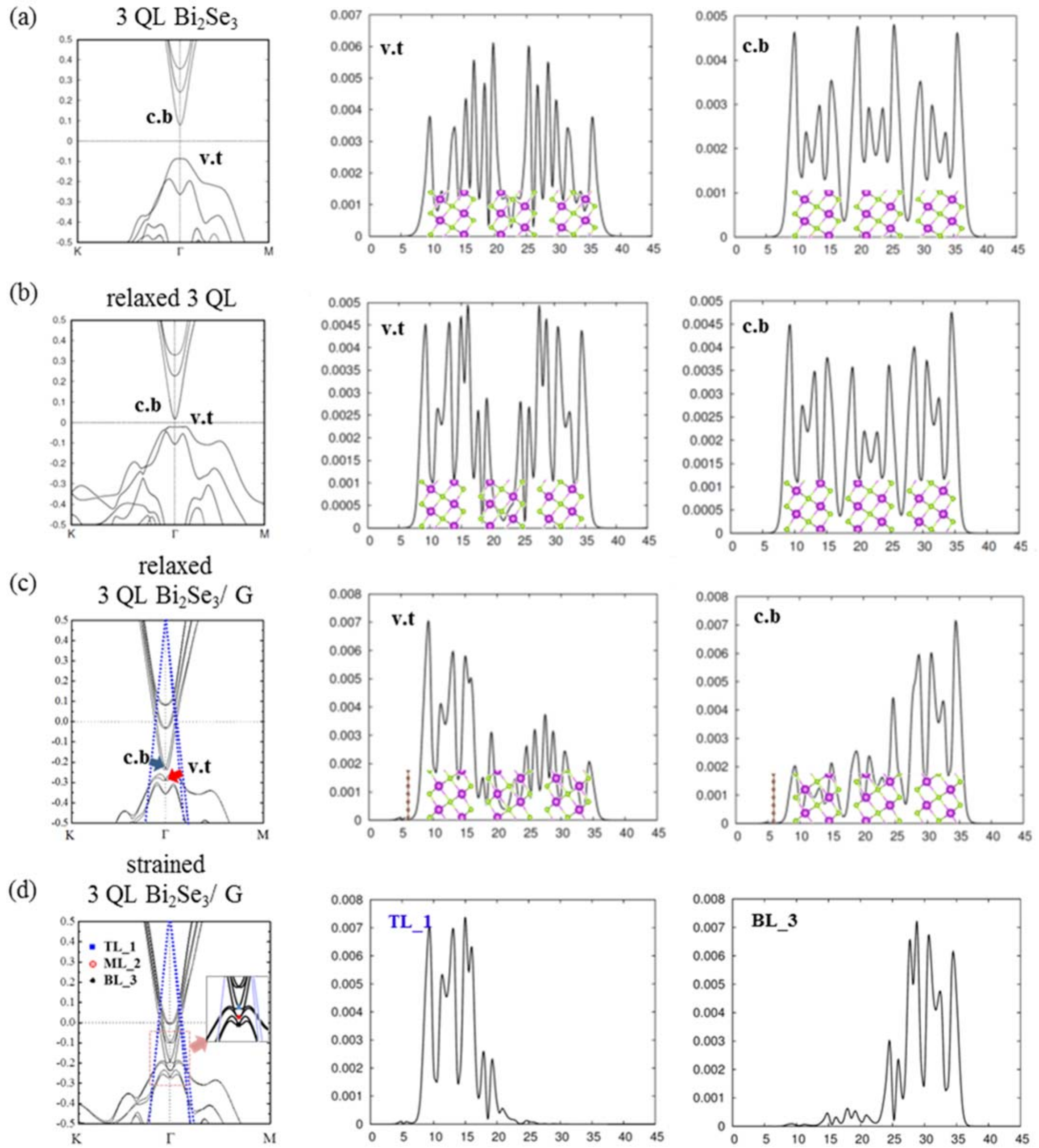

Figure S5. Band structures and their spatial distributions of (a) bare 3 QL Bi_2Se_3, (b) 3 QL Bi_2Se_3 considering the relaxed parameters in the Bi_2Se_3/graphene, (c) relaxed 3 QL Bi_2Se_3/graphene, and (d) strained 3 QL Bi_2Se_3/graphene. The graphene has linear bands as represented in (c) and (d) with blue dots

We plotted the spatial distribution of Bi_2Se_3 and Bi_2Se_3/graphene heterostructures. Both the conduction and valence band of bare Bi_2Se_3 are distributed throughout the whole film (figure S5 (a)). The spatial distribution in the strained 3QL Bi_2Se_3 is very similar to the bare 3 QL Bi_2Se_3 film (figure

S5 (b)). However, the conduction band and valence band in the samples with the graphene are divided at each top and bottom in both relaxed 3 QL Bi_2Se_3/graphene and strained 3QL Bi_2Se_3/graphene structure. This localization results from the band bending caused by graphene. It implies that breaking of the symmetry in Bi_2Se_3 film due to the charge transfer with the graphene induces the localization of the surface states and prevents the hybridization of surface states. In detail, without strain, each wavefunction of top and bottom surface state is distributed in a relatively large range in which a small wavefunction exists at the opposite layer. However, with strain of 2%, the wavefunctions of top and bottom surface states almost belong to each top and bottom layer. As a result, this separation of wavefunctions in strained 3 QL Bi_2Se_3/graphene heterostructure induces the complete bandgap closing of surface state.

6. Work function of graphene and Bi_2Se_3/graphene heterostructure

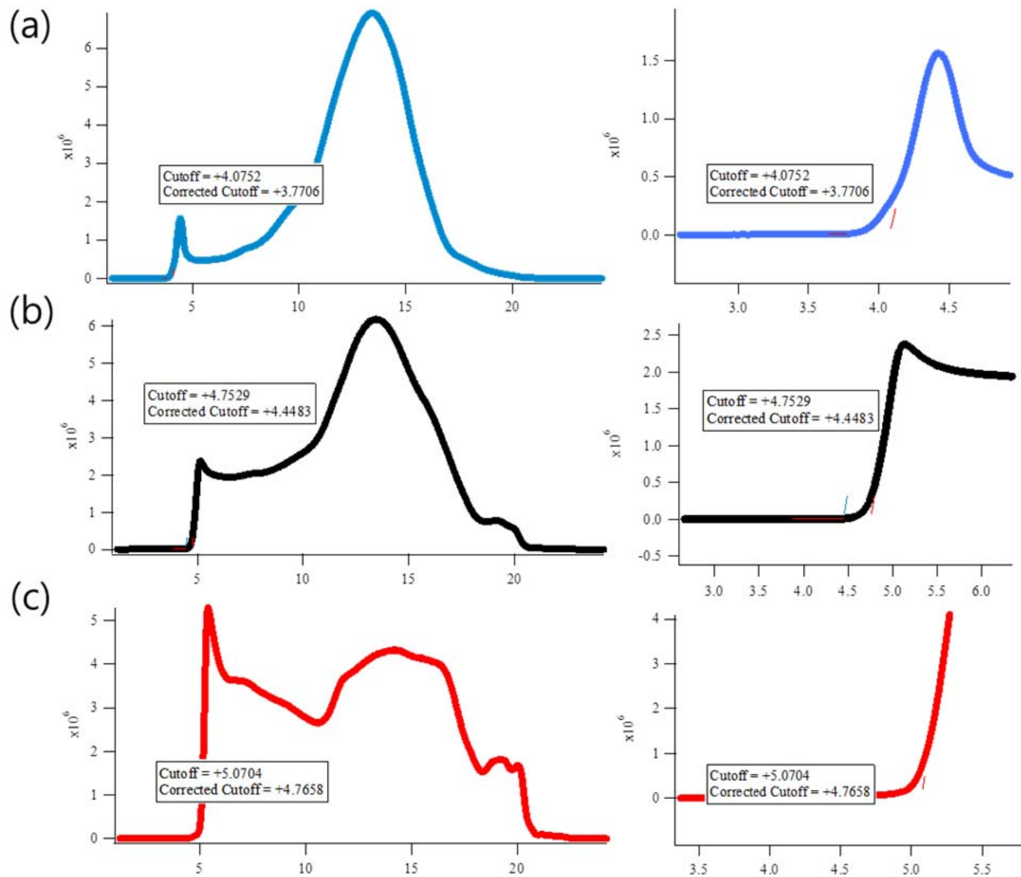

Figure S6. UPS spectra and secondary cutoff energy of (a) graphene grown on SiC substrate, (b) 3 QL Bi_2Se_3 on graphene/SiC substrate, and (c) 20 QL Bi_2Se_3 on graphene/SiC substrate.

The work functions of monolayer graphene, 3QL Bi_2Se_3/graphene, and 5 QL Bi_2Se_3/graphene on SiC substrates were measured by ultraviolet photoemission spectroscopy. Strong band bending occurs because of the large work function difference between the Bi_2Se_3 film (5.07 eV) and graphene/SiC substrate (4.075 eV), so that strong spatial localization of the surface state would occur, as we showed in the simulation data.

7. band structure as the strain increased

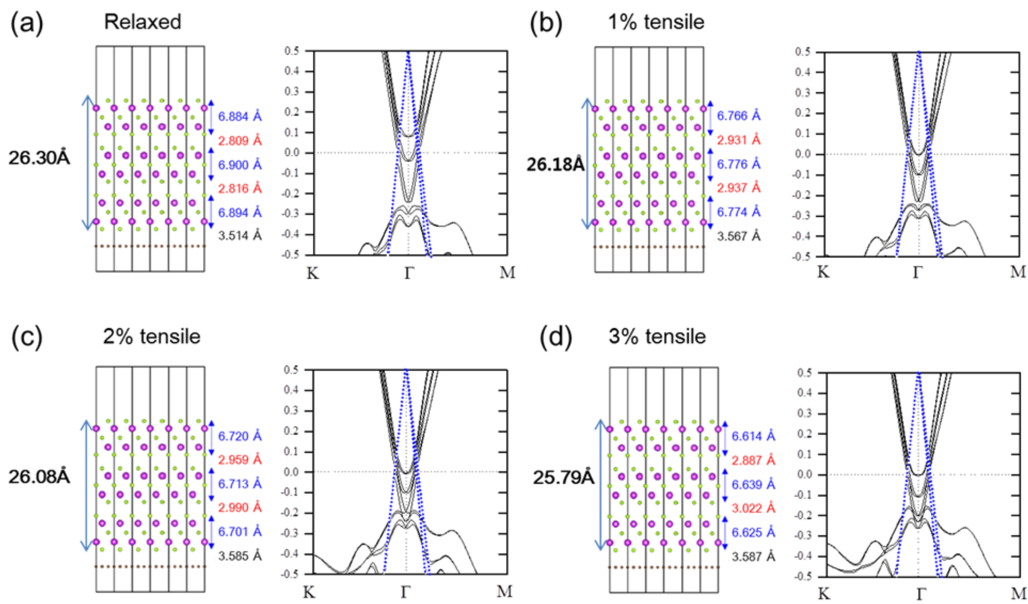

Figure S7. Band structures of (a) relaxed 3QL Bi_2Se_3/graphene and (b)–(d) 1 %–3 % tensile-strained 3 QL Bi_2Se_3/graphene in the in-plane direction. (e)–(h) the lattice parameters of the calculation.

We investigated the change in surface gap by increasing the tensile strain up to 3 % in DFT calculation. We observed the complete bandgap closing, using the DFT calculation, in the 3 QL Bi_2Se_3/graphene with 2% tensile strain in the in-plane direction. We plotted the relaxed 3 QL Bi_2Se_3/graphene and 1%, 2%, and 3% strained 3QL Bi_2Se_3, as shown in figure S7. Although the exact

lattice distance cannot be determined because the intralayer distance and vdW distance changes differently, the total distance between highest and lowest Se in 3 QL Bi_2Se_3 decreased from 26.30 Å to 26.08 Å (~0.8%). This is consistent with XRD results in which d-spacing of Bi_2Se_3/graphene/SiC is smaller within 1% than that of Bi_2Se_3/graphene/SiO_2. The total distance between highest and lowest Se decreases to 25.79 Å, which is approximately 2%. The two vdW distances (top layer to middle layer and middle layer to bottom layer) are different from each other, implying that the strain from graphene effect is too strong to make the Bi_2Se_3 film asymmetric. The bandgap is closed when the tensile strain in the in-plane direction increases to 2%. When 3 % strain is applied, the bandgap remains closed in the DFT calculation. Although the Dirac point moved to the bulk valence band, there is no notable difference in band structure compared with 2% strained 3 QL Bi_2Se_3/graphene, *i.e.*, as the strain exceeds 2%, the bandgap remains closed.

8. Magneto-conductance of 20 QL Bi_2Se_3 film

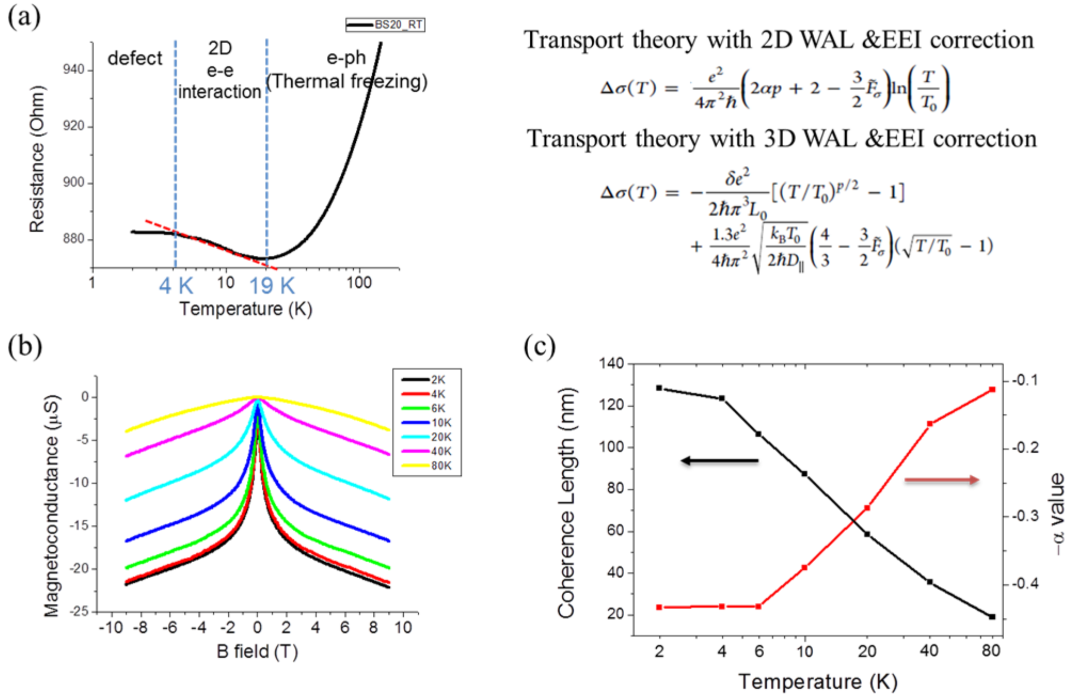

Figure S8. (a) Temperature dependent resistance and (b) magneto-conductance of 20 QL Bi_2Se_3 film. (c) temperature dependency of coherence length and α value determined by Hikami-Larkin-Nagaoka equation

We measured the magneto-conductance of the 20 QL Bi_2Se_3 film to verify the typical trends of Bi_2Se_3 films. For the temperature-dependent resistance (figure S8 (a)), there are three temperature regions, depending on the dominant scattering (or transport) mechanisms: electron-phonon interaction (> 19 K), two-dimensional electron-electron interaction (4 K < T < 19 K), and defect sites (< 4 K). Similar trends are observed in both Bi_2Se_3/graphene heterostructures (figure 4(a)). In addition, we obtained magneto-conductance as a function of temperature (figure S8 (b)). As we describe in the manuscript, clear WAL is observed, so we fitted the curve using the Hikami-Larkin-Nagaoka equation and found a temperature-dependent change in both α and l_{φ}.

9. Magneto-conductance as a function of temperature

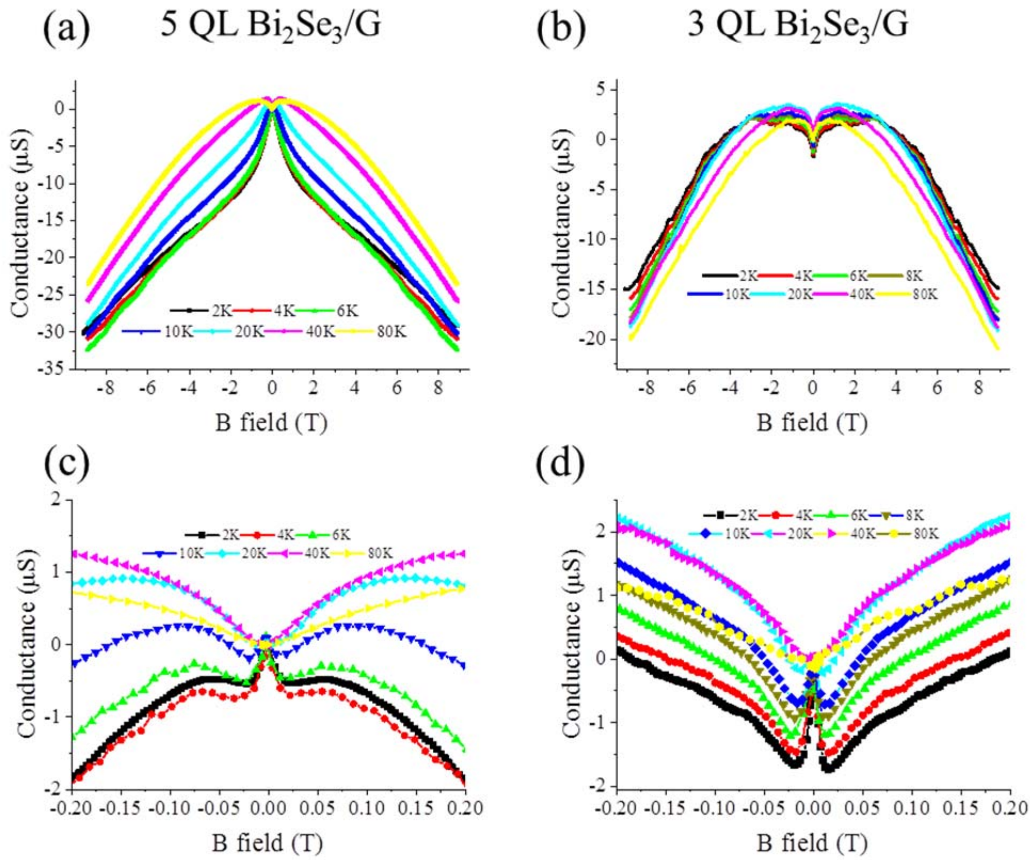

Figure S9. magneto-conductance data as a function of temperature for (a) 3 QL and (b) 5 QL Bi_2Se_3 grown on the graphene/SiO2 substrate. (c) and (d) are extended plots of (a) and (b), respectively.

The detailed magneto-conductance data as a function of temperature is shown in figure S9. The weak anti-localization (WAL) of graphene at high B-field is due to the graphene layer in both 3 QL and 5 QL Bi_2Se_3/graphene heterostructures. In figure S9 (a), typical weak anti-localization caused by the Bi_2Se_3 film in the range from 0.1 T to 1 T is observed more clearly than in figure 4 (b). As the temperature increases from 2 K, WAL from the Bi_2Se_3 weakens and is rarely seen over 40 K for the 5 QL sample (figure S9 (c)) and over 20 K for the 3 QL sample (figure S9 (d)), at which temperature the scattering mechanism changes from 2D electron-electron interaction to e-phonon interaction, as shown in figure 4 (a).

10. Detailed fitting of WAL and WL in the Bi_2Se_3/graphene heterostructures

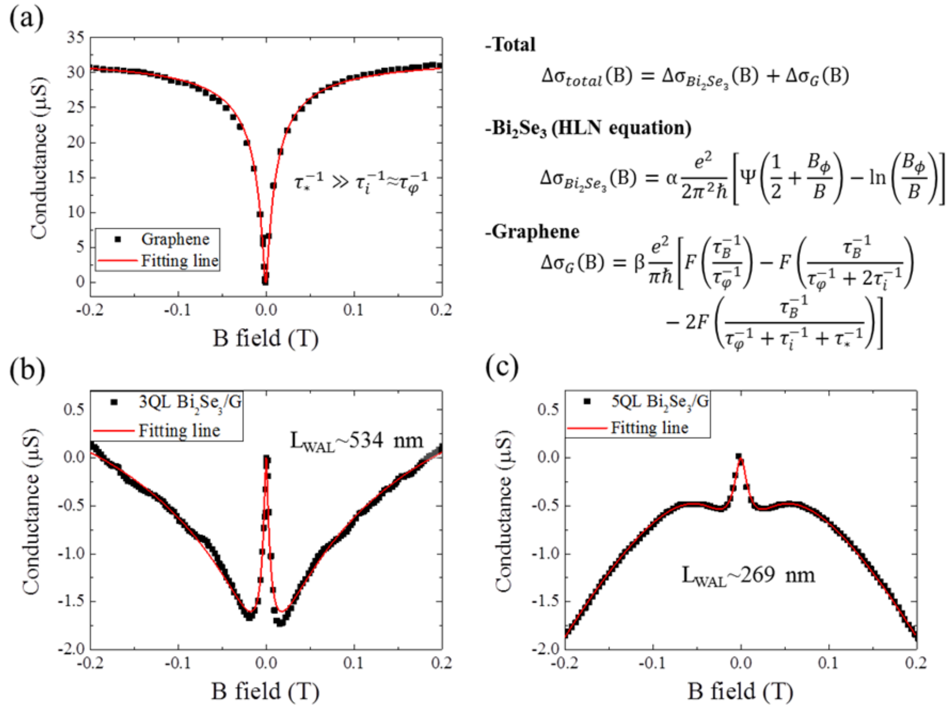

Figure S10. Fitting of (a) graphene, (b) 3 QL Bi_2Se_3/graphene heterostructure, and (c) 5 QL Bi_2Se_3/graphene heterostructures. Fitting was performed using both the simplified HLN equation for the WAL of topological insulators and the general equation for the WL of graphene.

We fitted the 3 QL Bi_2Se_3/graphene and 5 QL Bi_2Se_3/graphene heterostructures considering both transport channels of Bi_2Se_3 and graphene. The equations we used are as follows:

$$\Delta\sigma_{total}(\mathrm{B}) = \Delta\sigma_{Bi_2Se_3}(\mathrm{B}) + \Delta\sigma_G(\mathrm{B})$$

$$\Delta\sigma_{Bi_2Se_3}(\mathrm{B}) = \alpha\frac{e^2}{2\pi^2\hbar}\left[\Psi\left(\frac{1}{2}+\frac{B_\phi}{B}\right) - \ln\left(\frac{B_\phi}{B}\right)\right]$$

$$\Delta\sigma_G(\mathrm{B}) = \beta\frac{e^2}{\pi\hbar}\left[F\left(\frac{\tau_B^{-1}}{\tau_\varphi^{-1}}\right) - F\left(\frac{\tau_B^{-1}}{\tau_\varphi^{-1}+2\tau_i^{-1}}\right) - 2F\left(\frac{\tau_B^{-1}}{\tau_\varphi^{-1}+\tau_i^{-1}+\tau_*^{-1}}\right)\right]$$

where $\Psi(z)$ is a digamma function and $F(z) = lnz + \Psi(0.5+z^{-1})$. The coefficients α and β correspond to the prefactors for the TI film and graphene, respectively, considering the contribution for the conduction. $B_\phi = \hbar/4De\tau_{WAL}$ $\tau_B^{-1} = (4De/\hbar)B$, and τ_x^{-1} $(x = \varphi, i, *)$ are associated with phase-breaking (φ), inter-valley (i) and intra-valley ($*$) scattering, where τ_*^{-1} is divided into single valley chirality-breaking and trigonal warping rates. In addition, using the coherence lengths L_y^{-1} $(y = WAL, \varphi, i, *) = (D\tau_y)^{1/2}$, we can extract each coherence length of L_{WAL}, L_φ, L_i and L_* from the fitting data (we refer the phase coherence length l_φ in Bi_2Se_3 as L_{WAL} in order to avoid confusion with the phase coherence length L_φ of graphene).

For the Bi_2Se_3, we used the simplified HLN equation as we fitted the WAL of 20 QL Bi_2Se_3 films in figure S8; for the graphene, we used the general equation for the WL of graphene described by E. McCann[3]. Detailed fitting results are listed in table S1. The fitting results for the WL of the single-layer graphene, $L_\varphi = 434\,nm$, $L_i = 296\,nm$ and $L_* < 1$ nm, imply that there are strong scattering sources such as defects and grain boundaries in graphene. In the heterostructure of 3 QL Bi_2Se_3/graphene, strong WL was also found and the coherence lengths were lower than that of bare graphene. In 5QL Bi_2Se_3/graphene, WL became weak and the lengths were changed to reasonable values, in which τ_*^{-1} can be compared with other lengths ($\tau_\varphi^{-1} < \tau_i^{-1} < \tau_*^{-1}$). This implies that the quality of graphene could be improved in the stack structure of Bi_2Se_3/graphene, which is consistent with reported data[4]. The absolute values of coherence lengths were lower than the reported values for the graphene[5] because of the quality difference between exfoliated and CVD-grown films.

The prefactor α values in 3QL Bi_2Se_3/graphene and 5 QL Bi_2Se_3/graphene were found to have the same value of 0.18, which is lower than the ideal value of 0.5 for the surface conductance channel. This can be attributed to the Anderson localization, which is found in ultrathin and disordered TI films with low conductivity[6]. The phase coherence lengths of 3 QL Bi_2Se_3/graphene and 5 QL Bi_2Se_3/graphene, however, were found to have much higher values than other reported values, as we discussed in manuscript.

Table S1. Fitting values of WAL and WL in graphene, 3 QL Bi_2Se_3/graphene (BS/G) and 5 QL BS/G. We set β=1 for the fitting of WL in bare graphene.

	α	L_{WAL} or l_{φ}	β	$L_{g\varphi}$	L_i	L_*
Graphene	-	-	1	434	296	<1
3 QL BS/G	0.18	534	0.182	261	35	<1
5 QLBS/G	0.18	269	0.243	163	109	56.7

References

1. Zhang, Y.; He, K.; Chang, C. Z.; Song, C. L.; Wang, L. L.; Chen, X.; Jia, J. F.; Fang, Z.; Dai, X.; Shan, W. Y.; Shen, S. Q.; Niu, Q.; Qi, X. L.; Zhang, S. C.; Ma, X. C.; Xue, Q. K. Crossover of the Three-Dimensional Topological Insulator Bi_2Se_3 to the Two-Dimensional Limit. *Nat. Phys.* **2010,** *6*, 584-588.
2. Tarakina, N. V.; Schreyeck, S.; Borzenko, T.; Schumacher, C.; Karczewski, G.; Brunner, K.; Gould, C.; Buhmann, H.; Molenkamp, L. W. Comparative Study of the Microstructure of Bi_2Se_3 Thin Films Grown on Si(111) and InP(111) Substrates. *Cryst. Growth Des.* **2012,** *12*, 1913-1918.
3. McCann, E.; Kechedzhi, K.; Fal'ko, V. I.; Suzuura, H.; Ando, T.; Altshuler, B. L. Weak-Localization Magnetoresistance and Valley Symmetry in Graphene. *Phys. Rev. Lett.* **2006,** *97,*146805.
4. Lee, P.; Jin, K. H.; Sung, S. J.; Kim, J. G.; Ryu, M. T.; Park, H. M.; Jhi, S. H.; Kim, N.; Kim, Y.; Yu, S. U.; Kim, K. S.; Noh, D. Y.; Chung, J. Proximity Effect Induced Electronic Properties of Graphene on Bi_2Te_2Se. *ACS Nano* **2015,** *9*, 10861-10866.
5. Tikhonenko, F. V.; Horsell, D. W.; Gorbachev, R. V.; Savchenko, A. K. Weak Localization in Graphene Flakes. *Phys. Rev. Lett.* **2008,** *100,* 056802.
6. Liao, J.; Ou, Y. B.; Feng, X.; Yang, S.; Lin, C. J.; Yang, W. M.; Wu, K. H.; He, K.; Ma, X. C.; Xue, Q. K.; Li, Y. Q. Observation of Anderson Localization in Ultrathin Films of Three-Dimensional Topological Insulators. *Phys. Rev. Lett.* **2015,** *114, 216601*.